Ice-rich (periglacial) vs icy (glacial) depressions in the Argyre region, Mars: a proposed cold-climate dichotomy of landforms

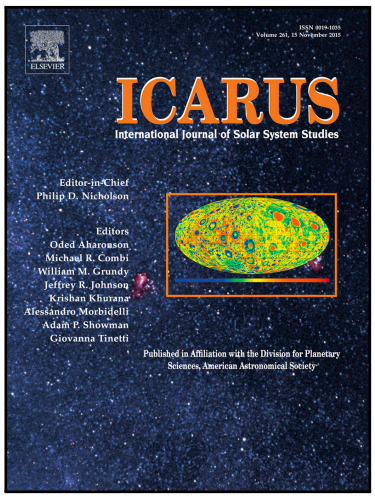

Ice-rich (periglacial) vs icy (glacial) depressions in the Argyre region, Mars: a proposed cold-climate dichotomy of landforms

R.J. Soare , S.J. Conway , C. Gallagher , J.M. Dohm

PII: S0019-1035(16)30571-1
DOI: 10.1016/j.icarus.2016.09.009
Reference: YICAR 12184

To appear in: *Icarus*

Received date: 16 December 2015
Revised date: 2 August 2016
Accepted date: 4 September 2016

Please cite this article as: R.J. Soare , S.J. Conway , C. Gallagher , J.M. Dohm , Ice-rich (periglacial) vs icy (glacial) depressions in the Argyre region, Mars: a proposed cold-climate dichotomy of landforms, *Icarus* (2016), doi: 10.1016/j.icarus.2016.09.009

Highlights

- Identification of ice-rich (periglacial) vs icy (glacial) “thermokarstic” depressions in the Argyre region.
- Evidence of regional pre-glacial “periglaciation”.
- Possible endogenic source of periglacial thermokarst.

Ice-rich (periglacial) vs *icy* (glacial) depressions in the Argyre region, Mars: a proposed cold-climate dichotomy of landforms

R.J. Soare[1], S.J. Conway[2-3], C. Gallagher[4], J.M. Dohm[5]

[1]Department of Geography,
Dawson College, Montreal, Canada, H3Z 1A4
(rsoare@dawsoncollege.qc.ca)

[2]Department of Physical Sciences,
Open University, Milton Keynes, United Kingdom, MK7 6AA

[3]Laboratoire de Planétologie et Géodynamique - UMR CNRS 6112, 2 rue de la Houssinière - BP 92208, 44322 Nantes Cedex 3, France.

[4]UCD School of Geography, University College, Belfield, Dublin 4, Ireland
[5]UCD Earth Institute, University College, Belfield, Dublin 4, Ireland

[6]The University Museum, The University of Tokyo,
Hongo 7-3-1, Bunkyo-ku, Tokyo 113-0033, Japan

Pages - 32

Figures - 9

Tables - 2

Keyword - Mars, climate; Mars, surface; Mars, polar geology

ABSTRACT

On Mars, so-called "scalloped depressions" are widely observed in Utopia Planitia (*UP*) and Malea Planum (*MP*). Typically, they are rimless, metres- to decametres-deep, incised sharply, tiered inwardly, polygonised and sometimes pitted. The depressions seemingly incise

terrain that is *icy* and possibly thermokarstic, i.e. produced by the thermal destabilisation of the icy terrain. Agewise, the depressions are thought to be relatively youthful, originating in the Late Amazonian Epoch.

Here, we report the presence of similar depressions in the Argyre region (*AR*) (30-60^0 S; 290-355^0 E). more importantly, we separate and differentiate these landforms into two groups: *ice-rich periglacial* depressions (Type-1); and, *icy glacial* depressions (Type-2a-c). This differentiation is presented to the Mars community for the first time.

Based on a suite of morphological and geological characteristics synonymous with *ice-complexes* in the Lena Peninsula (eastern Russia) and the Tuktoyaktuk Coastlands (Northwest Territories, Canada), we propose that the Type-1 depressions are *ice-rich* periglacial basins that have undergone volatile depletion largely by sublimation and as the result of thermal destabilisation. In keeping with the terms and associated definitions derived of terrestrial periglacial-geomorphology, *ice-rich* refers to permanently frozen-ground in which ice lenses or segregation ice (collectively referenced as *excess ice*) have formed.

We suggest that the depressions are the product of a multi-step, cold-climate geochronology:

1) Atmospheric precipitation and surface accumulation of an *icy* mantle during recent high obliquities.
2) Regional or local triple-point conditions and thaw/evaporation of the mantle, either by exogenic forcing, i.e. obliquity-driven rises of aerial and sub-aerial temperatures, or endogenic forcing, i.e. along Argyre impact-related basement structures.
3) Meltwater migration into the regolith, at least to the full depth of the depressions.
4) Freeze-thaw cycling and the formation of *excess ice*.

5) Sublimation of the *excess ice* and depression formation as high obliquity dissipates and near-surface ice becomes unstable.

The Type-2 depressions exhibit characteristics suggestive of *supra-glacial dead-ice basins* and *snow/ice suncups* observed in high-alpine landscapes on Earth, e.g. the Swiss Alps and the Himalayas. Like the Type-1 depressions, the Type-2 depressions could be the work of sublimation; however, the latter differ from the former in that they seem to develop within a glacial-like *icy* mantle that blankets the surface rather than within an *ice-rich* and periglacially-revised regolith at/near the surface.

Interestingly, the Type-2 depressions overlie the Type-1 depressions at some locations. If the periglacial/glacial morphological and stratigraphical dichotomy of depressions is valid, then this points to recent glaciation at some locations within the *AR* being precursed by at least one episode of periglaciation. This also suggests that periglaciation has a deeper history in the region than has been thought hitherto. Moreover, if the hypothesised differences amongst the Argyre-based depressions are mirrored in Utopia Planitia and Malea Planum, then perhaps this periglacial-glacial dichotomy and its associated geochronology are as relevant to understanding late period landscape-evolution in these two regions as it is in the *AR*.

1. Introduction

On Mars, depressions that are metre- to decametre-deep, polygonised (and sometimes pitted) depressions that are rimless, incised sharply, inwardly-terraced or stepped, and occasionally scalloped, are observed widely in Utopia Planitia (*UP*) (Costard and Kargel, 1995; Seibert and Kargel, 2001; Morgenstern et al., 2007; Soare et al., 2007, 2008, 2009; Lefort et al.,

2009a; Séjourné et al., 2011, 2012; Ulrich et al., 2010) and Malea Planum (*MP*) (Lefort et al., 2009b; Zanetti et al., 2010; Wilmes et al., 2012). The depressions are thought to: a) have formed in the very Late Amazonian Epoch, given the sharpness of their incision, the highly-muted terrain in which they occur, and sparse cratering; b) reside in *icy* terrain; and, c) be thermally destabilised and ice-depleted - *thermokarstic* - as the result of near-surface and obliquity-driven ice instability (Costard and Kargel, 1995; Morgenstern et al., 2007; Soare et al., 2007, 2008, 2009; Lefort et al., 2009a-b; Zanetti et al., 2010; Ulrich et al., 2010; Wilmes et al., 2012). Similar depressions are observed in and around the Argyre impact-basin region (*AR*) in the southern hemisphere (30-60^0 S; 290-355^0 E). Some workers suggest that this is a region where near-surface water ice and surface liquid-water could be meta-stable even under current conditions (Haberle et al., 2001; Zent et al., 1986, also, Hecht et al., 2002).

In the Lena Peninsula (eastern Russia) (e.g. Schirrmeister et al., 2002, 2013; Grosse et al., 2007) and the Tuktoyaktuk Coastlands (Northwest Territories, Canada) (e.g. Washburn, 1973; Mackay, 1979; Murton, 1996; Dallimore et al., 2000; Hill et al., 2001; French, 2007) depressions of the type observed in the *AR*, as well in *UP* and *MP*, often occur in *ice-complexes*. These complexes or landform assemblages are: *ice-rich* (i.e. containing *ice lenses* and *segregation ice*, collectively reference as *excess ice*, from metres to decametres of depth); incised by ice-wedge polygons and polygon trough/junction ponds or pits; punctuated by thermokarstic-terrain (i.e. terrain underlain by excess ice) and rimless depressions or *alases* (where the excess ice has been lost by evaporation or drainage) (e.g. Schirrmeister et al., 2002, 2013; Grosse et al., 2007).

Other depressions in the *AR* show morphologies and traits similar in some ways to those presented above; however, they are distinguishable by the absence of polygonisation, trough/junction pits and inward-oriented terraces and the presence of sharp rims (in some

instances), bowl-like shape and dense honeycomb-like clustering. Collectively, this second group of depressions is suggestive of *supra-glacial lake basins* and of *snow/ice suncups* as observed, for example, in the Swiss Alps (Kääb and Haeberli, 2001; Paul et al., 2007) and the Himalayas (Benn et al., 2000; Reynolds, 2000).

Supra-glacial lakes occur in debris-covered *dead-ice* (ice that has been decoupled from an originating glacier) (Kääb and Haeberli, 2001); here, irregularly-shaped crevasses formed by the stress of glacial advance and retreat fill with water, derived of melted snow or ice, and evolve into small metres-deep lakes that are metres to decametres in (long-axis) diameter (Kääb and Haeberli, 2001). Meltwater drainage or evaporation exposes floor or basin morphologies similar to those associated with the second group of Mars depressions. Small-sized polygons have not been reported in the terrain adjacent to the *dead-ice lakes* or *basins* on Earth.

Suncups comprise sharply-narrow and sub-metre high ridges separated by smoothly-concave sub-metre bowls or hollows (Betterton, 2001; Herzfeld et al., 2003); it is thought that they form by the differentiated albeit highly-localised ablation (sublimation or evaporation) of dirty vs clean snow (Betterton, 2001; Herzfeld et al., 2003; Mitchell and Tiedje, 2010).

In this article we have three main aims:

1) map the distribution of **(Fig. 1)** and describe the polygonised, tiered and sometimes-pitted depressions in the *AR*, defined as Type-1 depressions **(Fig. 2)**; discuss their morphological and geological synonymy with the thermokarst terrain on Earth where *ice-complexes* are observed **(Fig. 3)**; and, propose a possible periglacial-origin for these depressions.

2) map the distribution of **(Fig. 1)** and describe morphologically similar but unpolygonised, untiered and unpitted Type-2 depressions in the region **(Fig. 4)**; we

propose that these depressions are glacial in origin and analogous to alpine *dead-ice lake* basins and *suncups* on Earth **(Fig. 5)**.

3) hypothesise that an endogenic influence could be responsible, at least in part, for the thermal de-stabilisation required to form the Type-1 depressions.

Numerous studies have explored the possibility of freeze-thaw cycling of water affecting landscape changes throughout the *AR* during the Late Amazonian Epoch: a) clastically sorted, small-sized (≤~25 m in diameter) polygons (Banks et al., 2008; Soare et al., 2016); b) clastically unsorted, small-sized and low-centred polygons (Soare et al., 2014a); c) (possible) hydraulic or open-system pingos (Soare et al., 2014b); and, d) gelifluction-like lobes (Johnsson et al., 2015; Soare et al., 2015, 2016). The proposed dichotomy of landforms and associated geochronology presented here is consistent with this premise and underlines the extent to which relatively-recent boundary conditions in the *AR* might have be less uniformly cold and dry, perhaps even to the present day, than is generally thought.

2. Definition of key periglacial terms

The proposed differentiation of periglacial from glacial depressions in the Argyre region can be meaningful only in as much as the key referential or framing terms are identified and then defined clearly. Towards this end, the generally-accepted usage of these terms in terrestrial geology and periglacial-geomorphology is our benchmark. We recognise that some workers in the Mars community of planetary scientists believe that the relevance and viability of definitions derived of terrestrial systems or landscapes is contingent upon their adaptation to the Martian context (e.g. Byrne et al., 2009; Dundas et al., 2015; Sizemore et al., 2015). However, until a discrete and thorough discussion on appropriate periglacial-terms and -definitions for Mars appears in the scholarly literature, deference to the current lexicon of terrestrial geology and periglacial-geomorphology might be the most prudent course to plot.

2.1 Permafrost and excess ice

Permafrost, i.e. soil that has been frozen for at least two years, is *ice-rich* if and when it contains *excess ice* (Harris et al. 1988). *Excess ice* describes *permafrost* those pore space is exceeded by ice within that body; it comprises discrete *ice lenses* or lenses of *segregation ice* that range in thickness from hairline to >10m and, typically, are observed in alternating horizons of ice and soil (Penner, 1959; Harris et al., 1988). Fine-grained soils are particularly adept at forming *excess ice* because their small pores and pathways induce the movement of unfrozen water to the freezing front at a rate commensurable with the formation of *ice lenses* (Penner, 1959; Harris et al., 1988). Frost settlement or deflation occurs when *excess ice* thaws and meltwater pools or is removed from the thaw site is lost by evaporation or drainage (Washburn, 1973; French, 2007).

2.2 Thermokarst

Generically, terrain that comprises *ice-rich* permafrost and, is subject to frost settlement or deflation is referenced as *thermokarst* (e.g. Washburn, 1973, Harris et al. 1988, Murton, 1996; Dallimore et al., 2000; French, 2007) **(Fig. 3a)**. An *alas* is the depression formed by the surface/near-surface and localised loss of *excess ice* (Harris et al., 1988). If this loss produces a pond and, subsequently, if the ponded water evaporates or drains episodically, inwardly-oriented and scalloped-shaped benches or terraces may develop on the basin margins **(Fig. 3b)**.

The shape (sub-circular to elongate), size (metres to kilometres in long-axis diameter), depth (sub- to multi-metres) and distribution (individually, clustered or coalesced) of *thermokarst* landforms mirror the vertical and horizontal distribution of *ice-rich permafrost* in a landscape and the penetration reach of a thermal wave (e.g. Washburn, 1973, Harris et al. 1988, Murton, 1996; French, 2007). Terrain punctuated by the presence of *excess ice* is particularly

sensitive to disturbance and volumetric loss if or when seasonal or annual mean-temperatures rise substantially (e.g. Washburn, 1973; Mackay, 1992; Hill et al., 2001; French, 2007).

2.3 Thermal-contraction polygons

Often, *thermokarstic* terrain is incised by small-sized (generally ≤25 m in diameter) and non-sorted (thermal-contraction) polygons (e.g. Mackay, 1972, 1992; Rampton, 1988; Hill et al., 2001; Kääb and Haeberli, 2001) **(Fig. 3b-f)**. Thermal-contraction fracturing is the result of tensile stresses in frozen ground induced by the sharp drop of sub-zero (0^0C) temperatures (Lachenbruch, 1962; Harris et al., 1988). Thermal-contraction fractures or cracks neither entail nor require the availability of liquid water (Lachenbruch, 1962). However, ice wedges and eventually, ice-wedge polygons, may form in thermal-contraction cracks when, where and when surface-meltwater migrates and freezes *in situ*.

If these ice wedges thaw, meltwater may pool and then pond within the marginal troughs and junctions that bound the polygons **(Figs. 3c-f)**. Impelled by thermal erosion, the ponds sometimes grow and evolve into small-scale fluvio-lacustrine systems or streams that have a beaded appearance **(Figs. 3d)** (e.g. Hopkins et al., 1955; Washburn, 1973; Black, 1976; Harris et al., 1988; French, 2007). They are beaded, as melt-water pools more substantially at polygon junctions than within polygon troughs, and systemic, in as much as the polygon troughs connect or link individual pools or beads to one another (Washburn, 1973; Harris et al., 1988; French, 2007).

3. Methods

In order to identify possible mantle-incising periglacial and glacial depressions within the *AR*, we performed a systematic survey of the available HiRISE (High Resolution Imaging Science Experiment) images (n=1044) that cover the region (30-60°S; 290-355°E) **(Fig. 6)**. We

excluded depressions that present characteristics consistent with impact craters, i.e. completely circular with a raised rim (whether ejecta were present or not). HiRISE images are between 25 and 50 cm/pix; they have sufficient resolution to identify the geological context of these depressions. One of the key-observations that motivated our wider survey was that the depressions seemingly show different morphologies depending on whether or not they are spatially associated with polygonally-patterned ground. The presence or absence of metre-scale polygonally patterned ground can be ascertained with confidence only at the resolution of HiRISE images. Therefore, although many of the depressions included in this study are visible in Mars Orbiter Camera, Narrow Angle (MOC-NA; ~1.5 m/pix) or Mars Reconnaissance Orbiter Context (CTX; 6 m/pix) images, the associated features cannot be identified; hence they are not encompassed in this study.

We use two methods to estimate depression depths. One or the other method was employed in an opportunistic fashion when the data were available. Firstly, where the depressions are large enough (at least twice the Mars Orbiter Laser Altimeter (MOLA) shot-spacing, ~300 m) and if they are also crossed by MOLA tracks, these cross sections are used to estimate depression depth, as follows. We fit a plane to the points on either side of the depression (or on one side if both sides were not made of the same material) and measure the maximum vertical-distance between this plane and the MOLA shot located at the lowest elevation within the depression. Secondly, where the depressions are small we use shadow measurements to estimate depression depths; however, because such depressions have very shallowly-sloping walls we perform this analysis only where images are taken with high solar-incidence angles.

Shadow measurements are performed according to the method presented in (Dauber et al., 2014). Briefly, shadows cast by depression walls are measured along the solar azimuth on the

RDR HiRISE image and then converted to height (*h*) by assuming a flat-floored depression and then applying the following formula: $h = l_m / \sqrt{(\tan^2 i + \tan^2 e - 2 \tan i \tan e \cos v)}$ where l_m is the measured length, *i* is the incidence angle, *e* is the emission angle and *v* is the subsolar azimuth. It should be noted that for the majority of the images surveyed, we were not able to apply either of these methods, because of the limitations of these methods, mentioned above.

4. Observations

4.1 Type-1 depressions

Of the 1044 HiRISE images that cover the *AR* we report twenty-five locations where the Type-1 depressions are observed **(Fig. 1; Table 1)**. These locations overlie thirteen disparate geological-units that range in age from the late Noachian to the late Hesperian Epochs. Six of the fourteen locations (cf. Table 1, # 14-15, 17-20) are (~48.8-55.6^0 S; 297.5-307.5^{0}E) are amidst or adjacent to a geological corridor linking Argyre Planitia to a large basin on its western flank in the cratered highlands. Dohm et al. (2015) refer to this basin as the Argyre western-margin paleolake (*AWMP*). Here, linear margins and tectonic structures are widespread; this points to the possibility of impact-related basement-control of the surface geology (Dohm et al., 2015). Otherwise, the distribution of the Type-1 depressions shows no apparent latitudinal-constraint or gradient as one would expect were obliquity-driven climate the dominant control of depression formation **(Fig. 1; Table 1)**.

The Type-1 depressions **(Fig. 2a-h)** display various plan-forms: circular **(Fig. 2b)** or sub-circular **(Fig. 2c-d)**, tear-dropped **(Fig. 2f)** and, occasionally, scalloped, exhibiting inward-oriented tiers or terraces **(Fig. 2d)**. They are observed individually **(Fig. 2b)**, clustered **(Fig. 2c-d)** or coalesced, sometimes in wave-like (planform) patterns of distribution **(Fig. 2e)**. Depression-length (long axes of the depressions defined by the outermost closed-contour line)

ranges from ~85-1000 m; widths range from ~50-500 m. Depression-depths reach ~40m (**Figs. 7a-b**); however, it should be noted that we are able to identify only two sites where the depressions are significantly larger than the MOLA shot spacing and are crossed by MOLA tracks. Collectively, we ascertain no preferred geographical-orientation amongst individual depressions, although this could be an artefact of the small sample-size. However, where the depressions coalesce, each of them display the same (long-axis) orientation **(e.g. Figs. 2c-d)**. Depression margins are continuous albeit rimless, well defined and, often, relatively sharp **(Figs. 2c-d)**. Generally, depression floors are sloped gently and their gain or loss of elevation follows the local topography **(Figs. 7a-b)**. Some floors, however, are uneven and are covered in part by rocky debris and boulders **(Fig. 2c)**.

In all of the Type-1 depressions identified by us, depression-margins, -sides, -floors and even the terrain beyond the depressions themselves, are incised by small-sized (~5 m) and non-sorted polygons **(e.g. Figs. 2b-g; cf. Table 1**). Many of these polygons comprise centres surrounded by marginal metre to sub-metre (diameter) troughs and trough-junctions **(Fig. 2g)**. Some of the intra-depression polygonal troughs and junctions are pitted **(Fig. 2g)**. These pits are circular to sub-circular and measure a metre or more in diameter **(Fig. 2g)**. Where the pits are slightly larger than this, the shape of the underlying troughs and/or junctions is distorted, even obscured **(Fig. 2g)**.

Some pits are connected; this gives them the appearance of linked beads **(Fig. 2g)**. Occasionally, the connected pits display metre-wide and fan-like features that overtop the trough margins (**Fig. 2h**). Overall, there seems to be no uniform orientation of pit or trough alignment; both north-south (or south-north) **(Fig. 2g)** and west-east (or east-west) orientation **(Fig 2g)** are commonplace, although as noted above with regard to the Type-1 depressions themselves, this

could be an artefact of the small sample-size. Where the pits and cavities are clustered, the surrounding terrain may form a slight depression **(Fig. 2g)**.

Typically, the depressions are embedded in a smooth (and relatively light-toned) mantle that mutes the underlying terrain and topography **(Fig. 8a)**. Mantle depth ranges from metres to decametres **(Figs. 7a-b)**. Impact craters are sparse and boulders/rocky terrain are scarce where the mantle is continuous and relatively thick. Where the depression-dissected mantle is discontinuous and relatively thin, rocky terrain may be observed adjacent to the mantle. The latter, invariably, exhibits no depressions **(Fig. 8b)**. At some locations the polygonised Type-1 mantle seemingly underlies the Type-2 mantle **(Fig. 4f)**.

4.2 Type 2 depressions

Overall, the observed Type-2(a-c) depressions are more numerous than the Type-1 depressions and are located largely to the north of 50^0 S **(Fig. 1; Table 2)**. The Type-2(a) depressions are decametre to kilometre in scale and copy the diverse morphology of Type-1 depressions **(Figs. 4a-c)**, except for the absence of scalloped rims, tiered interior slopes, wave-like planform or interior polygonal-patterning.

Like the Type-1 depressions, the Type-2(a) depressions are rimless; they are also anchored in mantled terrain that is relatively smooth **(Figs. 4b, d-e)**, cratered sparsely and absent of boulders/rocky terrain; however, unlike the Type-1 depressions, neither the 2(a) depressions nor the terrain incised by them are polygonised at any of the locations observed by us **(Figs. 4a-c)**.

Type-2(b) depressions comprise multi-metre to decametre-scale pits that are shaped irregularly and rimmed sharply **(Figs. 4c-d, f)**. These pits or hollows occur in dense clusters that exhibit a honeycomb-like appearance and, often, reside within Type-2(a) depressions. The 2(b)

depressions, like the 2(a) depressions, show smooth textures that are not polygonised. As noted in the previous section, some Type-2(b) depressions and the Type-2 mantle incised by them appear to overlie a Type-1 mantle, the latter being identified by its polygonisation **(Fig. 4f)**.

The Type-2(c) depressions, similarly to the 2(b) depressions, are shaped irregularly, have raised-rims and display diameters in the multi-metre to decametre range **(Figs. 4g-h)**. Where the distribution of these depressions is dense and ubiquitous, as it may be throughout the inter-crater plains of the region, the depressions impart a sponge-like texture to the landscape **(Figs. 4g-h)**. The ubiquity of these depressions enables us to estimate their depths using shadow-measurements on low sun-angle images. For Table 2-location 22 (ESP_026851_1445, solar incidence 76.7°) we made 100 random measurements of shadows cast by the walls of the depressions; depression depths range from 0.5-4.7m and the average depth is 2.3 m **(Fig. 9a)**. For Table 2-location 27 (ESP_028552_1440, solar incidence 66.892612°) we made 30 random measurements; depression depths range from 0.6-3.2 m and the average depth is ~1.6 m **(Fig. 9b)**. The Type-2(c) depressions are observed on impact-crater ejecta (**Fig. 4i**); terrain adjacent to the ejecta **(Fig. 4i)**; and, as noted above, expansively on inter-crater terrain.

4.3 Type-1 depressions: uniquely different from Type-2 depressions

In the main, there are five key traits or characteristics that differentiate the Type-2(a-c) from the Type-1 depressions. First, the Type-1 depressions are polygonised, as is the terrain adjacent to the depressions; by means of contrast, the Type-2 depressions are unpolygonised in all observed instances, as is the terrain adjacent to them. Second, the Type-1 depressions exhibit pitting, sometimes beaded, within polygon-margin troughs and trough-junctions. Pitting of this type is not observed in conjunction with any of the Type-2 depressions. Third, some of the Type-1 depressions, especially those that exhibit wave-like clustering, are scalloped and show inward-

oriented tiers or terraces; none of the observed Type-2 depressions exhibit similar traits. Fourth, the bowl-like and multi- to decametre-wide Type-2(b) depressions often are nested within the Type-2(a) depressions but never within the Type-1 depressions. Fifth, where the Type-2 and Type-1 mantles (and their spatially-associated depressions) are observed concurrently in a landscape the Type-1 mantle underlies the Type-2 mantle in all instances.

5. Type-1 depressions and possible ice-rich (periglacial) complexes

The spatial-synonymy of the Type-1 depressions and the (sometimes) pitted, (invariably) polygonised-terrain in the Argyre region (within and adjacent to the Type-1 depressions) mirrors that of thermokarst/alas assemblages and polygon-margin pits in periglacial, *ice -rich complexes* on Earth. As noted above, the latter develop a) when and if *excess ice* is present in the near-surface permafrost, sometimes to decametres of depth; and, b) when and if the *excess ice* undergoes heat-induced thermal destabilisation and is removed from the permafrost by evaporation or drainage.

The possible origin and loss of *excess ice* as a precursive condition to the formation of Type-1 depressions is neither simple nor straightforward. In order to frame our hypothesis aptly, we propose a (simplified) four-step meteorological and geological chronology. It coalesces generally-accepted assumptions concerning obliquity-related *icy* mantle formation in the Late Amazonian Epoch with the requirements of forming an *ice-complex* derived of freeze-thaw cycles in periglacial landscapes on Earth. *Ice complexes* formed entirely by means of vapour-diffusion cycles have yet to be observed on Earth.

(Step-1): A water- or dusty-ice mantle forms at the mid to high latitudes of both hemispheres; it is the obliquity-driven product of atmospheric precipitation and surface accumulation (e.g. Mustard et al., 2001; Milliken et al., 2003; Head et al., 2003, 2006; Tanaka et

al., 2005; Forget et al., 2006; Madeleine et al., 2009, 2014; Schorghofer and Forget, 2012). This mantle predates the very Late Amazonian Epoch mantle commonly referenced in the literature by these and other workers but would be consistent with the origin, composition, landscape characteristics and geographical distribution of the current mantle discussed by them.

The observed and deduced evidence favouring an *icy* composition for the later mantle in the *AR* is as follows: (1) the elevated occurrence of near-surface water ice (inferred from the Mars Odyssey gamma-ray and neutron-spectrometer data); (2) landforms whose morphology collectively implies a glacial landscape, i.e. moraine- and esker-like ridges, lobate-debris aprons (i.e. possible debris covered rock-glaciers) and semi-circular (cirque-like) embayments; (3) the latitudinal constraint/distribution of the observed mantled-terrain, predicted by models linking ground-ice stability with recent changes in the obliquity and spin parameters of Mars (Banks et al., 2008, 2009; Wilmes et al., 2010; Zanetti et al., 2012; El Maarry et al., 2013).

(Step-2): As Mars moves towards high obliquity the early or antecedent mantle thaws and generates meltwater, especially in areas such as the *AR* where water could be metastable even under current conditions (e.g. Haberle et al., 2001; Zent et al., 1986; also, see Hecht, 2002); mantle thaw also could be produced endogenically were deeply-seated heat to be delivered to the surface by means of Argyre (impact-related) geothermal pathways, identified by linear margins and tectonic structures at the surface (Dohm et al., 2015; Williams et al., 2016; also, Soare et al., 2014).

(Step-3): The meltwater migrates into the underlying fine-grained regolith (Soare et al., 2016) and undergoes episodic freeze-thaw iterations at discrete and disparate freezing-fronts. This forms multiple *ice lenses* or layers. Basaltic regolith, thought to be commonplace in the *AR*

(e.g. Bandfield and Rogers, 2008), would be an ideal medium for this type of preferential freeze-thaw cycling and the formation of *excess ice*.

(Step-4): The ice degrades or ablates, probably by sublimation, as high obliquity wanes (e.g. Morgenstern et al., 2007; Lefort et al., 2009a-b; Séjourné et al., 2011, 2012) or in response to highly-localised endogenic forcing (Dohm et al., 2015); alas-like Type-1 depressions are formed. Subsequently, thermal-contraction cracking polygonises the depressions and the surrounding terrain (Costard and Kargel, 1995; Seibert and Kargel, 2001; Mangold et al., 2005; Levy et al., 2009). In turn, small-scale pits and linked beaded-troughs form within polygon margins; this could be the work of near-surface ice being removed from the regolith by sublimation or thaw/evaporation (Wan Bun Tseung and Soare, 2006; Soare et al., 2008; Séjourné et al., 2010; 2011, 2012).

6. Type-2 depressions and a high-alpine (glacial) analogue

A follow-up cycle of *icy* mantle-formation and -degradation occurs in the more recent past. As the mantle forms it blankets the terrain in which the polygonised Type-1 depressions developed and subsequently, at an indeterminately later time, begins to sublimate; dead-ice (like) basins and snow/ice suncups are an end-product of this sublimation (Massé et al., 2010; Mangold, 2011). Further degradation ablates the mantle sufficiently to expose the underlying Type-1 depressions, as well as the polygonised terrain that incises and encompasses them.

7. Discussion and conclusion

On the basis of disparate morphological-traits, trait-assemblages and landscape-characteristics we have identified two different depression-types (Type-1 and Type-2) in the *AR*. We propose that the first depression-type approximates (periglacial) *alases* on Earth, whereas the

second type exhibits striking similarities with terrestrial (supra-glacial) *dead-ice basins* and *suncups*.

The glacial pathway that produces the Type-2 depressions is somewhat simpler than the one associated with the periglacial formation of the Type-1 depressions; it is also largely consistent with the widely-held beliefs about obliquity-driven mantle formation and degradation in the Late Amazonian Epoch. Moreover, the plausibility of the glacial pathway is not contingent upon triple-point conditions being reached.

By means of contrast, the periglacial pathway that engenders the formation of the Type-2 depressions requires multiple episodes of freeze-thaw cycling (perhaps facilitated by the presence of brines in the regolith), antecedent mantle-formation and -degradation, and the accumulation of *excess ice* to decametres of depth.

Some preliminary work has explored a possible formation-pathway for near-surface *ice lenses* and *excess ice* based on absorption/diffusion cycles (Dundas, 2015; Sizemore, 2015). However, whether this pathway is robust enough to form excess ice to the depths associated with the largest of the Type-1 (alas-like) depressions is an open question.

The observed superposition of the Type-2 mantle and associated depressions on polygonised Type-1 terrain suggests that discrete and multiple episodes of relatively-recent mantle formation can be identified, separated stratigraphically, and linked to disparate cold-climate origins. It also highlights the possibility that significant thermokarstic-revisions of the regional landscape in the *AR* predate the most recent period of glaciation.

Interestingly, some of the Type-1 depressions exhibit polygon-junction and trough-pitting as well as some small-scale beading comprised of interconnected polygon-junction and polygon-trough pits. Similar morphologies are observed in *ice-rich* landscapes on Earth and are diagnostic

of: a) antecedent polygonised ice-wedging; b) ice thaw; c) the formation, ponded accumulation and eventual evacuation of ice-derived meltwater by evaporation or drainage; and, d) the organisation of localised fluvio-lacustrine (periglacial) systems. At some locations small fan-like features overtop the beaded troughs; this points to the possibility of highly-localised debris flow.

The relative absence of uniformity in the orientation of the junction-pit linked-assemblages argues against the possibility of formation by aeolian deflation (Morgenstern et al., 2007; Séjourné et al., 2010) or by tectonic/structural forces (Lefort et al., 2009a). But even if the pits and beading are the work of sublimation, not evaporation or drainage, the morphologies of the pits and beads points strongly towards the presence of near-surface ground-ice, a key marker of an ice-rich landscape.

The absence of an apparent latitudinal-constraint on the distribution of the Type-1 depressions, as well as the paucity of the Type-1 depressions compared to the Type-2 depressions, is enigmatic. Under current or recent aerial or sub-aerial boundary conditions, ice stability is thought to increase with latitude (e.g. Mellon and Jakosky, 1995; Head et al., 2003; Morgenstern et al., 2007; Lefort et al., 2009b; Zanetti et al., 2010; Dundas, 2015). If the ascription of a thermokarstic origin to the Type-1 depressions is valid, then one would expect the number of Type-1 depressions to decrease with latitude, in line with an increase of ice stability.

On the other hand, the small number of observed Type-1 depressions could be the result of highly-localised and favourable surface-pressures and temperatures in the *AR* when the depressions formed, as could be inferred from Haberle et al., (2001) and Zent et al., (1986), also Hecht (2002).

An endogenic origin of thermal instability ought not to be discounted either. A few Type-1 depressions are clustered in the area of the *AWMP*. Here, linear margins and tectonic structures

are widespread and, as noted above, some recent work has hypothesised a connexion between deeply-seated heat, possible impact-related geothermal pathways and ice instability at/near the surface in this and other areas of the *AR* (Dohm et al., 2015; Williams et al., 2016; also, Soare et al., 2014).

Lastly, the surface coverage of the Argyre impact-basin floor by the *HiRISE* imagery is poor and small in scale. Perhaps the small population of observed Type-1 depressions is simply an artefact of this poor coverage.

However, were the presumed differences between the two depression-types in the *AR* valid and mirrored in Utopia Planitia and Malea Planum, then perhaps the commonly-held belief that the *UP* and *MP* depressions are rooted directly in an *icy* mantle ought to be revisited.

References

Bandfield, J.L., Rogers, A.D., 2008. Olivine dissolution by acidic fluids in Argyre Planitia, Mars: evidence for a widespread process? Geology 36, 7, 579-582, doi:10.1130/G24724A.1.

Banks, M.E., et al., 2008. High resolution imaging science experiment (HiRISE) of glacial and periglacial morphologies in the circum-Argyre Planitia highlands, Mars. Journal of Geophysical Research 113, E12015, doi:10.1029/2007JE002994.

Benn, D.I., Wiseman, S., Warren, C.R., 2000. Rapid growth of a supraglacial lake, Ngozumpa Glacier, Khumbu Himal, Nepal, in Nakawo, M., Raymond, C.F., and Fountain, A., (eds.). Debris-Covered Glaciers, IAHS publication 264, 177-185.

Betterton, M.D., 2001. Theory of the structure formation in snowfields motivated by penitentes, suncups, and dirt cones. Physical Review E, 63, 056129, 1-12, doi:10.1103/PhysRevE.63.056129.

Black, R.F., 1976. Features indicative of permafrost. Annual Review of Earth and Planetary Sciences 4, 75-94.

Byrne, S. et al., 2009. Distribution of mid-latitude ground ice on Mars from new impact craters. Science 325, 5948, 1674-1676, doi:10.1126/science.1175307.

Costard, F.M., Kargel, J.S., 1995. Outwash plains and thermokarst on Mars. Icarus 114, 1, 93-112, doi:10.1006/icar.1995.1046.

Dallimore, A., Schröder-Adams, C.J., Dallimore, S.R. 2000. Holocene environmental history of thermokarst lakes on Richards Island, Northwest Territories, Canada: thecamoebians as paleolimnological indicators. Journal of Paleolimnology 23, 261-283.

Dauber, I.J., Atwood-Stone, C., Byrne, S., McEwen, A.S., Russell, P.S., 2014. The morphology of small fresh craters on Mars and the Moon. Journal of Geophysical Research: Planets 119, 2014JE004671, doi:10.1002/2014JE004671

Dohm, J.M., et al., 2015. Geological and hydrological histories of the Argyre Province, Mars, 253, 66-98 Icarus doi:10.1016/j.icarus.2015.02.017.

Dundas, C., Byrne, S., McEwen, A.S., 2015. Modeling the development of Martian sublimation thermokarst landforms. Icarus 262, 154-169, dx.doi.org/10.1016/j.icarus.2015.07.033

Federov, A.N., Gavrilev, P.P., Konstantinov, P.Y., Hiyama, T., Iijima, Y., Iwahana, G., 2014. Estimating the water balance of a thermokarst lake in the middle of the Lena River basin, eastern Siberia. Ecohydrology 7, 188-196, doi:10.1002/eco.1378.

Forget, F., Haberle, R.M., Montmessin, D., Levrard, B., Head, J.W., 2006. Formation of glaciers on Mars by atmospheric precipitation at high obliquity. Science 311, 368, doi:10.1126/ science/1120335.

French, H.M., 2007. The periglacial environment, 3rd ed., J. Wiley & Sons, West Sussex,

England, 458 p.

Grosse, G., Schirrmeister, L., Siegert L., Kunitsky, V.K., Slagoda, E.A., Andreev, A.A., Dereviagyn, A.Y., 2007. Geological and geomorphological evolution of a sedimentary periglacial landscape in Northeast Siberia during the Late Quaternary. Geomorphology 86, 25-51.

Haberle, R.M., McKay, C.P., Schaeffer, J., Cabrol, N., Grin, E.A., Zent, A.P., Quinn, R. 2001. On the possibility of liquid water on present day Mars. Journal of Geophysical Research 106, E10, 23,317-23,326.

Harris, S.A., French, H.M., Heginbottom, J.A., Johnston, G.H., Ladanyi, B., Sego, D.C., van Everdingen, R.O., (eds.), 1988. Glossary of permafrost and related ground-ice terms. Technical Memorandum 142, Permafrost Subcommittee, National Research Council of Canada, 154 p.

Head, J.W., Mustard, J.F., Kreslavsky, M.A., Milliken, R.E., Marchant, D.R., 2003. Recent ice ages on Mars. Nature 426, 797-802, doi:10.1038/nature02114.

Head, J.W., Marchant, D.R., Agnew, M.C., Fassett, C.I., Kreslavsky, M.A., 2006. Extensive valley glacier deposits in the northern mid-latitudes of Mars: Evidence for Late Amazonian obliquity-driven climate change. Earth and Planetary Science Letters 241, 663-671, doi:10.1016/j.epsl.2005.11.016.

Hecht, M.H., 2002. Metastability of liquid water on Mars. Icarus 156, 373-286, doi:10.1006/icar.2001.6794.

Herzfeld, U.C., Mayer, H., Caine, N., Losleben, M., Erbrecht, T., 2003. Morphogenesis of typical winter and summer snow surface patterns in a continental alpine environment. Hydrological Processes 17, 619-649, doi:10.1002/hyp.1158.

Hill, P.R., Lewis, C.P., Desmarais, S., Kauppaymuthoo, V., Rais., H., 2001. The Mackenzie Delta: sedimentary processes and facies of a high-latitude, fine-grained delta. Sedimentology 48, 1047-1078.

Hopkins, D.M., Karlstrom, T.N.V., Black, R.F., Williams, J.R., Péwé, T.L., Fernold, A.T., Muller, E.H., 1955. Permafrost and ground water in Alaska, a shorter contribution to general geology; a study of the interrelations of permafrost and ground water, and a discussion of the role of aerial photographs in the mapping and evaluation of permafrost conditions. Geological Survey Professional Paper 264-F, Washington, D.C., United States Government Printing Office, 70 p.

http://www.ultralight backpacker.com/index.html, Joe's ultralight backpacking.

Johnsson, A., Reiss, D., Conway, S.J., Hauber, E., Hiesinger, H., 2015. Small-scale lobes in the southern hemisphere on Mars: implications for transient liquid water in the recent past. European Planetary Science Congress, Nantes, France, 10, 882.

Kääb, A., Haeberli, W., 2001. Evolution of a high mountain thermokarst lake in the Swiss Alps. Arctic, Antarctic and Alpine Research 33, 4, 385-390.

Lachenbruch, A.H., 1962. GSA Special Paper 70. Geological Society of America, New York, 69p.

Lefort, A., Russell, P.S., McEwen, A.S., Dundas, C.M., Kirk, R.L., 2009a. Observations of periglacial landforms in Utopia Planitia with the High Resolution Imaging Science Experiment (HiRISE). Journal of Geophysical Research 114, E04005, doi:10.1029/ 2008JE003264.

Lefort, A., Russell, P.S., Thomas, N., 2009b. Scalloped terrains in the Peneus and Amphrities

Paterae of Mars as observed by HiRISE. Icarus 205, 1, 259-268, doi:10.1016/j.icarus. 2009.06.005.

Levy, J., Head, J.W, Marchant, D.R., 2009. Thermal contraction crack polygons on Mars: Classification, distribution and climatic implications from HiRISE observations. Journal of Geophysical Research 114, E01007, doi:10.1029/2008JE003273.

Mackay, J.R., 1972. The world of underground ice. Annals of the Association of American Geographers 62, 1, 1-22.

Mackay, J., 1979. Pingos of the Tuktoyaktuk Peninsula, Northwest Territories, Géographie physique et quaternaire 33, 1, 3-61.

Mackay, J.R., 1992. Lake stability in an ice-rich permafrost environment: examples from the western Arctic coast. In R. D. Robarts & M. L. Bothwell (eds), Aquatic Ecosystems in Semi-arid Regions: Implications for Resource Management. N.H.R.I. Symposium Series 7, Environment Canada, Saskatoon, Canada, 1–22.

Madeleine, J-B., Forget, F., Head, J.W., Levrard, B., Montmessin, F., Millour, E., 2009. Amazonian northern mid-latitude glaciation on Mars: a proposed climate scenario. Icarus 203, 390-405, dx.doi.org/10.1016/j.icarus.2009.04.037.

Madeleine, J-B., Head, J.W., Forget, F., Navarro, T., Millour, E., Spiga, A., Colaitis, A., Määttänen, A., Montmessin, F., Dickson, J.L., 2014. Recent Ice Ages on Mars: The role of radiatively active clouds and cloud microphysics. Geophysical Research Letters 41, 14, 4873-4879, doi:10.1002/2014GL059861.

Mangold, N. 2005. High latitude patterned grounds on Mars: classification, distribution and climatic control. Icarus 174, 336-359, doi:10.1016/j.icarus.2004.07.30.

Mangold, N., 2011. Ice sublimation as a geomorphic process: a planetary perspective.

Geomorphology 126, 1-17, doi:10.1015/geomorph.2010.11.009.

Massé, M., Bourgeois, O., Le Mouélic, S., Verpoorter, C., Le Deit, L., Bibring, J.P., 2010. Martian polar and circum-polar sulfate-bearing deposits: sublimation tills derived from the North Polar Cap. Icarus, 209, 2, 434-451, doi:10.1016/j.icarus.2010.04.017.

Mellon, M., Jakosky, B.M., 1995. The distribution and behavior of martian ground ice during past and present epochs. Journal of Geophysical Research 100, E6, 11781-11799.

Milliken, R.E., Mustard, J.F., Goldsby, D.L., 2003. Viscous flow features on the surface of Mars: Observations from high-resolution Mars Orbiter Camera (MOC) images. Journal of Geophysical Research 108, E6, 5057, doi:10.1029/2002JE002005.

Mitchell, K.A., Tiedje, T., 2010. Growth and fluctuations of suncups on alpine snowpacks. Journal of Geophysical Research 115, F04039, doi:10.1029/2010JF001724.

Morgenstern, A., Hauber, E., Reiss, D., van Gasselt, S., Grosse, G., Schirrmeister, L., 2007. Deposition and degradation of a volatile-rich layer in Utopia Planitia, and implications for climate history on Mars. Journal of Geophysical Research 112, E06010, doi:10.1029/2006JE002869.

Murton, J., 1996. Thermokarst-lake basin sediments, Tuktoyaktuk Coastlands, western arctic Canada. Sedimentology 43, 737-760.

Mustard, J.F., Cooper, C.D., Rifkin, M.R., 2001. Evidence for recent climate change on Mars from the identification of youthful near-surface ground ice. Nature 412, 411-414. doi:10.1038/35086515.

Paul, F., Kääb, A., Haeberli, W., 2007. Recent changes in the Alps observed by satellite: consequences for future monitoring strategies. Global and Planetary Change 56, 111-122.

Penner E., 1959. The mechanism of frost heaving in soils. Highway Research Board, Bulletin

225, 1-22.

Rampton, V.N., 1988. Quaternary Geology of the Tuktoyaktuk Coastlands, Northwest Territories, Geological Survey of Canada, Memoir 423, 98 p.

Reynolds, J.M., 2000. On the formation of supraglacial lakes on debris-covered glaciers, in Nakawo, M., Raymond, C.F., and Fountain, A., (eds.). Debris-Covered Glaciers, IAHS publication 264, 153-164.

Robbins, S.J., Hynek, B.M., 2012. A new global data base of Mars impact craters ≥ 1 km. Database creation, properties, and parameters. Journal of Geophysical Research 117, E5, doi:10.1029/2011JE003966.

Robbins, S.J., Hynek, B.M., Lillis, R.J., Bottke, W.F., 2013. Large impact crater histories of Mars: the effect of different model crater age techniques. Icarus 225, 173-184, doi.org/10. 1016/j.icarus.2013.03.01.

Schirrmeister, L., Siegert, C., Kunitszky, V.V.,Grootes, P.M., Erlenkeuser, H., 2002. Late Quaternary ice-rich permafrost sequences as a paleoenvironmental archive for the Laptev Sea Region in northern Siberia. International Journal of Earth Sciences 91, 154-167.

Schirrmeister, L., Froese, D., Tumskoy, V., Grosse, G., Wetterich, S., 2013. Yedoma: Late Pleistocene ice-rich syngenetic permafrost of Beringia, in, Elias., S.A., (ed.) The Encyclopaedia of Quaternary Science 3, 542-552. Amsterdam: Elsevier.

Schorghofer, N., Forget, F., 2012. History and anatomy of subsurface ice on Mars. Icarus 220, 1112-1120, doi:10.1016/j.icarus.2012.07.003.

Seibert, N.M., Kargel, J.S., 2001. Small-scale martian polygonal terrain: implications for liquid surface water. Geophysical Research Letters 28, 5, 899-902.

Séjourné, A., Costard, F., Gargani, J., Soare, R.J., Marmo, C., 2010. The polygon junction pits as

evidence of a particularly ice-rich area in Utopia Planitia, 41st Lunar and Planetary Science Conference, Houston, Texas, 2113.

Séjourné, A., Costard, F., Gargani, J., Soare, R.J., Fedorov, A., Marmo, C., 2011. Scalloped depressions and small-sized polygons in western Utopia Planitia: a new formation hypothesis. Planetary and Space Science 59, 412-422, doi:10.1016/j.pss.2011.01.007.

Séjourné, A., Costard, F.N., Gargani, J., Soare, R.J., Marmo, C., 2012. Evidence of an eolian ice-rich and stratified permafrost in Utopia Planitia, Mars. Planetary and Space Science 60, 348-254, doi:10.1016/j.pss.2011.09.004.

Sizemore, H.G., Zent, A.P., Rempel, A.W., 2015. Initiation and growth of Martian ice lenses. Icarus 251, 191-210, doi:org/10.1016/j.icarus.2014.04.013.

Soare, R.J., Kargel, J.S., Osinski, G.R., Costard, F., 2007. Gully formation, periglacial processes and evidence of near-surface ground-ice in Utopia and western Elysium Planitia. Icarus 191, 1, 95-112, doi:10.1016/j.icarus.2007.04.018.

Soare, R.J., Osinski, G.R., Roehm, C.L., 2008. Thermokarst lakes and ponds on Mars in the very recent (late Amazonian) past. Earth and Planetary Science Letters 272, 1-2, 382-393, doi:10.1016/j.epsl.2008.05.10.

Soare, R.J., Osinski, G.R., 2009. Stratigraphical evidence of late Amazonian periglaciation and glaciation in the Astapus Colles region of Mars. Icarus 202, 1. 17-21. doi:10.1016/j. icarus.2009.02.009.

Soare, R.J., Séjourné, A., Pearce, G., Costard, F., Osinski, G.R., 2011. The Tuktoyaktuk Coastlands of northern Canada: A possible ‘‘wet’’ periglacial analogue of Utopia Planitia, Mars. In: Garry, W.B., Bleacher, J.E. (Eds.), Analogs for Planetary Exploration. Geological Society of America Special Paper 483. doi:10.1130/2011.2483(13).

Soare, R.J., Conway, S.J., Séjourné, A., Dohm. J.M., 2012. Climate change & the origin of ice-rich permafrost in mid Utopia Planitia, Mars. Mars Recent Climate Change Workshop, NASA Ames Research Centre, Moffett Field California. Abstract #

Soare, R.J., Conway, S.J., Dohm, J.M., 2014a. Possible ice-wedge polygons and recent landscape modification by "wet" periglacial processes in and around the Argyre impact basin, Mars. Icarus 233, 214-228, doi.org/10.1016/j.icarus.2014.01.034.

Soare, R.J., Conway, S.J., Dohm, J.M., El-Maarry, M.R., 2014b. Possible open-system (hydraulic) pingos in and around the Argyre impact region of Mars. Earth and Planetary Science Letters 398, 25-36, doi:10.1016/j.epsl.2014.04.044.

Soare, R.J., Horgan, B., Conway, S.J., Souness, C., El-Maarry-M.R., 2015. Volcanic terrain and the possible periglacial formation of "excess ice" at the mid-latitudes of Utopia Planitia, Mars. Earth and Planetary Science Letters 423, 182-192, doi.org/10.1016/j.epsl.2015.04.033

Soare, R.J., Conway, S.J., Gallagher, C., Dohm, J.M., 2016. Sorted (clastic) polygons in the Argyre region, Mars, and possible evidence of pre- and post-glacial periglaciation in the Late Amazonian Epoch. Icarus 264, 184-197, doi:10.1016/j.icarus.2015.09.019.

Ulrich, M., Morgenstern, A., Günther, F., Reiss, D., Bauch, K.E. Hauber, E., Rössler, S., Schirrmeister, L., 2010. Thermokarst in Siberian ice-rich permafrost: Comparison to asymmetric scalloped depressions on Mars. Journal of Geophysical Research 115, E10009, doi:10.1029/2010JE003640.

Wan Bun Tseung, J.M., Soare, R.J., 2006. 37th Lunar and Planetary Science Conference, Houston, Texas, 1414.

Washburn, A.L., 1973. Periglacial processes and environment. New York, NY, St Martin's

Press, 320 p.

Williams, J.P., Pathare, A., Dohm, J.M., Lopes, R.M.C., Buczkowski, D.L., 2016. Volcanism and giant polygons within the Argyre Basin, Mars, 47th Lunar and Planetary Science Conference, Abstract 2423.

Wilmes, M., Reiss, D., Hiesinger, H., Zanetti, M., 2012. Surface age of the ice-dust mantle deposit in Malea Planum, Mars. Planetary and Space Science, 60, 199-206, dx.doi.org/ 1016/j.pss.2011.08.006.

Zanetti, M., Hiesinger, H., Reiss, Hauber, E., Neukum, G., 2010. Distribution and evolution of scalloped terrain in the southern hemisphere, Mars. Icarus 206, 691-706, doi:10.1016/j. icarus.2009.09.010.

Zent, A.P., Fanale, F.P., Salvail, J.R., Postawko, S.E., 1986. Distribution and state of H_2O in the high-latitude shallow subsurface of Mars, Icarus, 67, 19-36.

Acknowledgements

RJS thanks Dawson College, in particular, D. Gauvin and L. Bennett, for a professional development leave that enabled him to present some of the ideas in this article precursively at the Nantes EPSC in October, 2015.

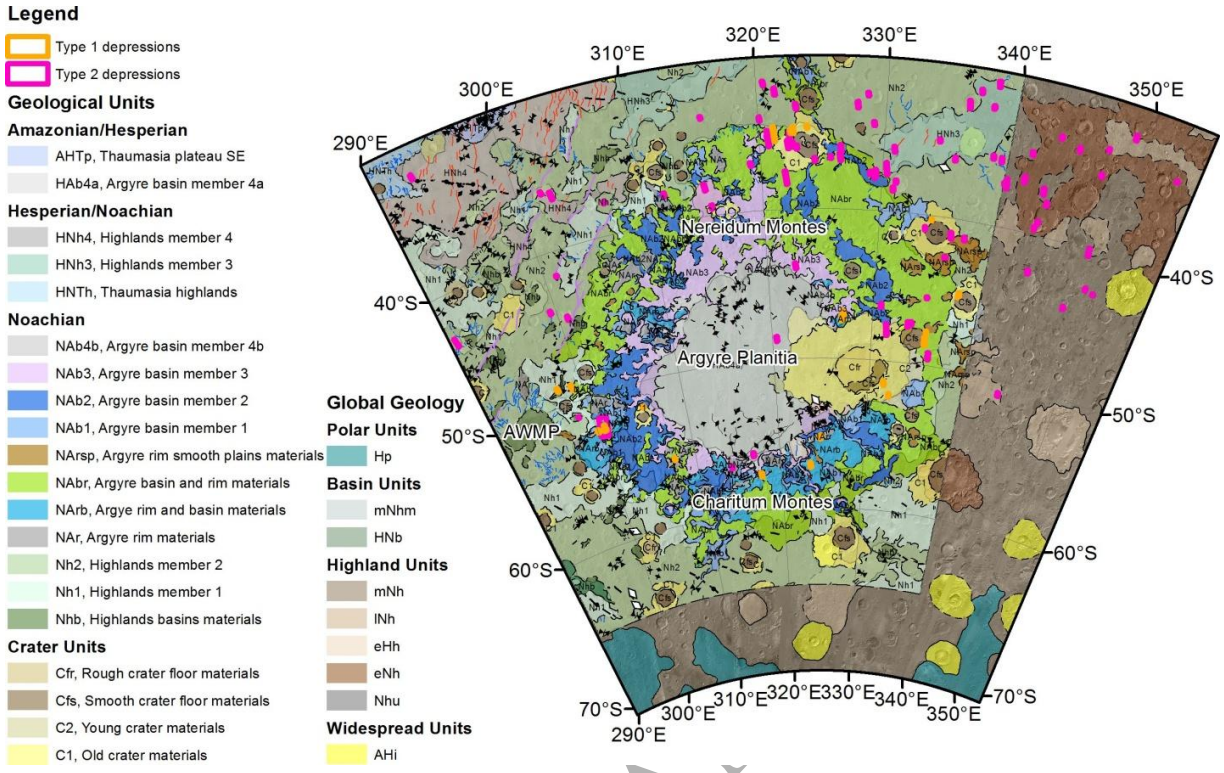

Fig. 1 Geological-unit map of the Argyre impact-crater and surrounding region of Mars (adapted from Dohm et al., 2015). The global geological-map is shown for areas outside of the Dohm et al. (2015) map. Type-1 depressions highlighted in orange; Type-2 depressions (shown in Fig. 4) highlighted in pink.

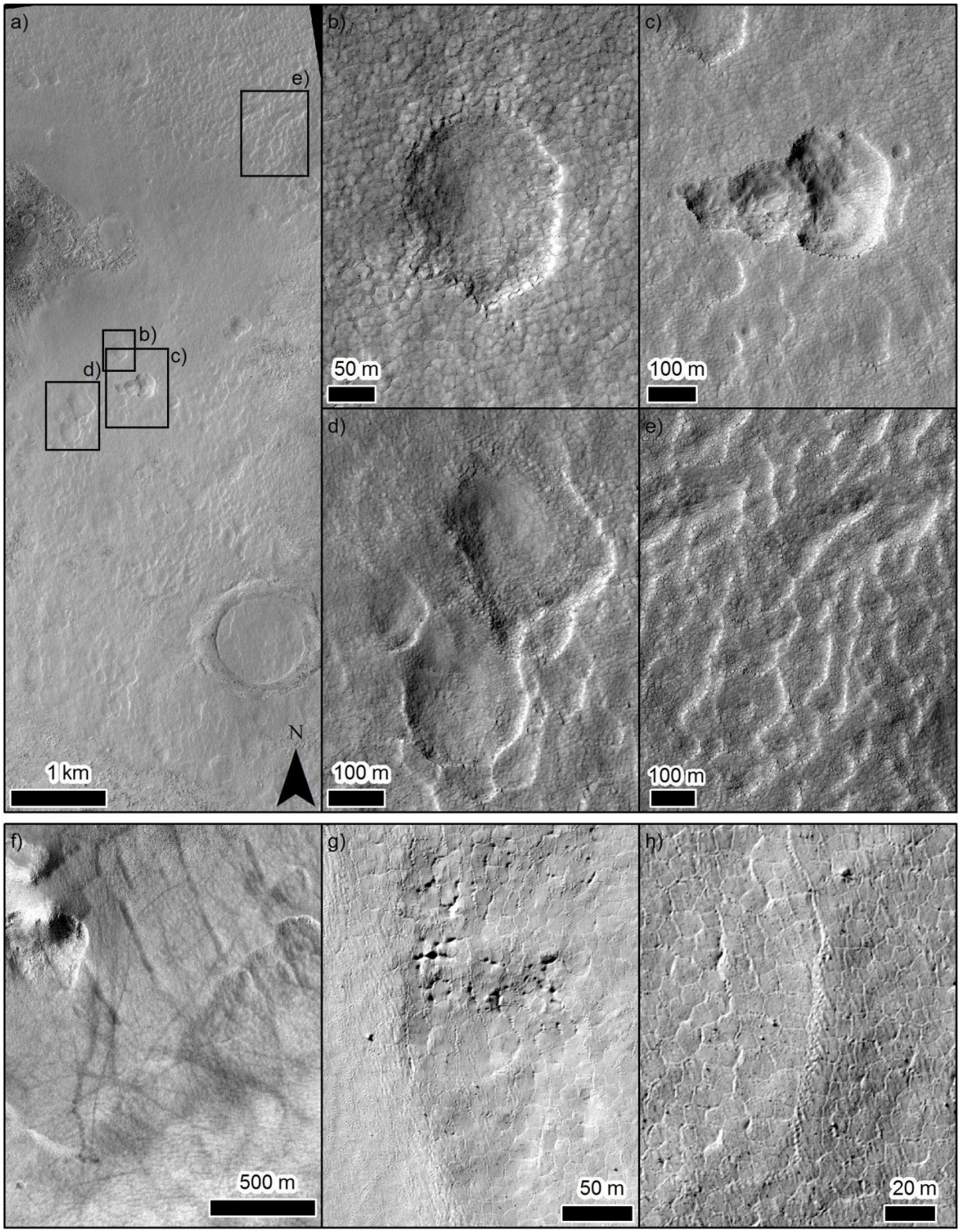

Fig. 2 (a) Type-1 (depression) morphologies and distribution (context-image). **(b)** Circular depression. Note the polygonised terrain surrounding the depression and the polygonised

depression-walls and -floors. **(c)** Four coalesced (sub-circular) depressions. Note the E/W or W/E latitudinal orientation of their collective long axes. **(d)** Sub-circular depressions that exhibit coalescence, scalloping and some wave-like (planform) distribution **(e)** Coalesced depressions with more extensive wave-like distribution (**a-e**: HiRISE image ESP_011319_1305; 298.954^{0}E, 49.001^{0}S; res. 50cm/pixel; NASA/JPL/University of Arizona). **(f)** Tear-drop shaped depression with longitudinally-orientated long-axis (HiRISE image ESP_013890_1240; 307.523^{0}E, 55.615^{0}S; res. 50cm/pixel; NASA/JPL/University of Arizona). **(g)** Depression with pitted and deformed polygon-margin troughs and junctions. Note the clustering and branching of these features (HiRISE image PSP_006176_1225.323.637^{0}E, 57.130^{0}S; res. 50cm/pixel; NASA/JPL/University of Arizona). **(h)** Polygon troughs with N/S orientation overtopped by small fan-like structures (HiRISE image PSP_006176_1225).

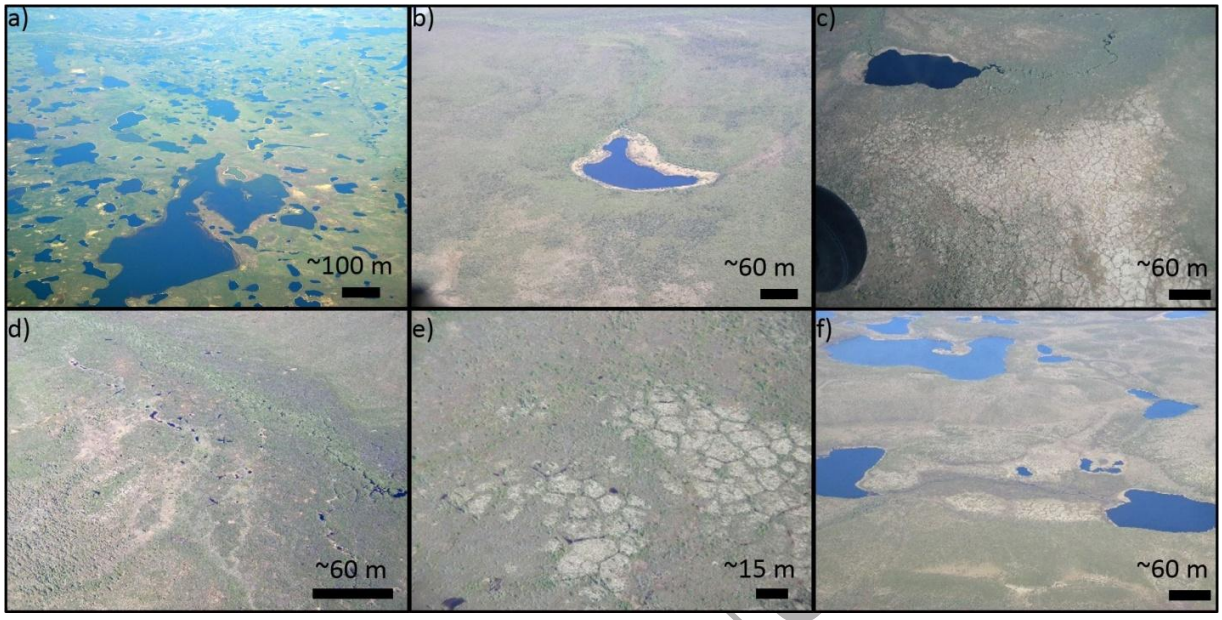

(a) Fig. 3 Thermokarst lake/alas (light-coloured and unvegetated patches of terrain) assemblages in the Tuktoyaktuk Coastlands. **(b)** Archetypal recession of a thermokarst-lake margin and the associated scalloping of that margin. **(c)** Thermokarst lake/alas assemblage. Note, 1. the receding lake-margin (top-left corner) and the subsequential polygonisation of the newly exposed lake-basin floor; and 2. the formation of a beaded fluvial-channel that meanders through interconnected polygon-margins at the right flank of the thermokarst lake. **(d)** Development of landscape-wide fluvial systems by means of interconnected polygon-troughs. **(e)** Small-scale pooling of meltwater at polygon margins on alas floors. **(f)** Convergence of pools and the formation of meltwater ponds. All air-photos are of the Tuktoyaktuk Coastlands (Northwest Territories, Canada) between Inuvik and Tuktoyaktuk. Image credits: R. Soare.

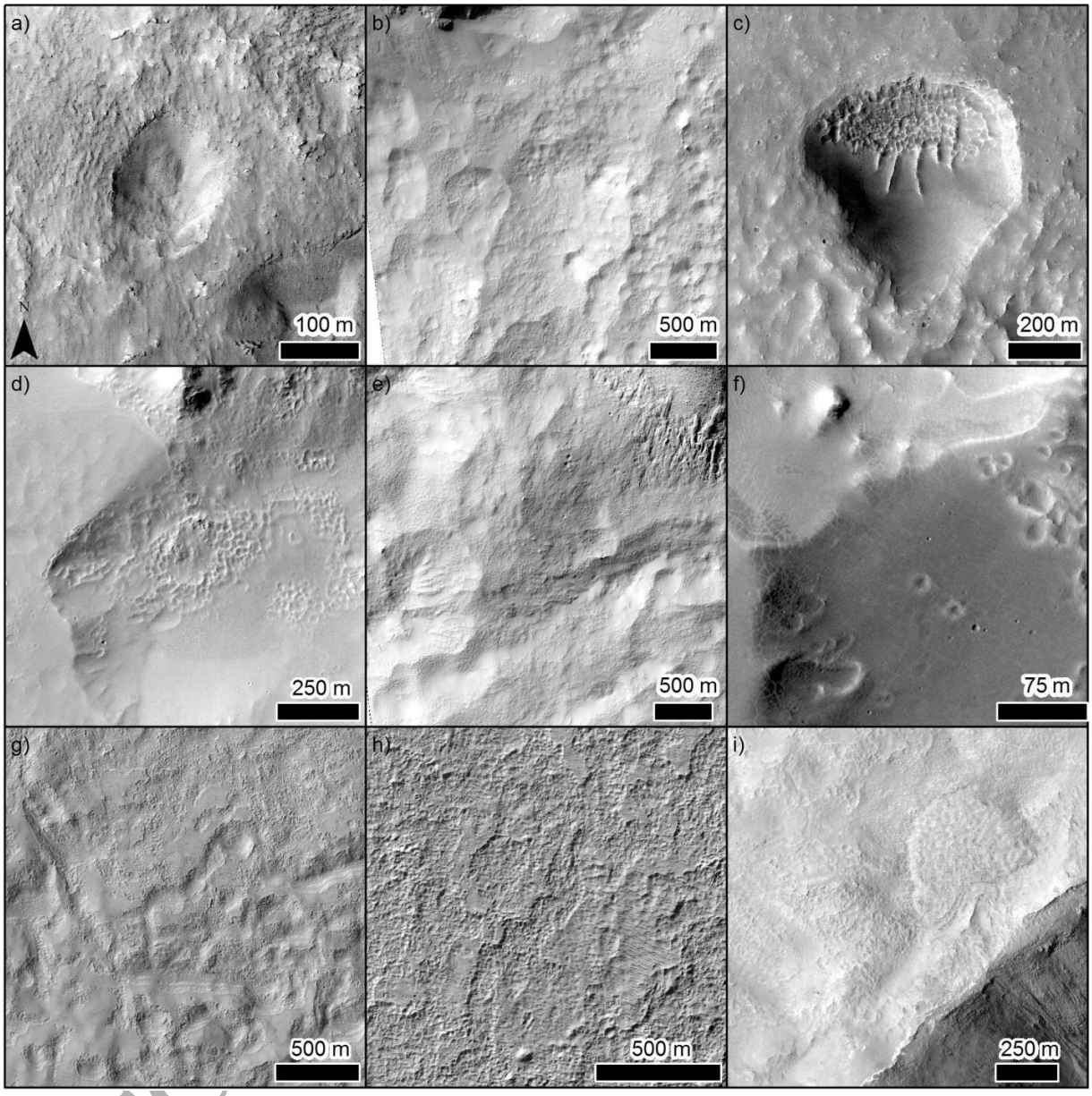

Fig. 4 (a-c) Type 2(a) depressions: circular, sub-circular and tear-dropped; rimless; and, decametres hundreds of metres in diameter (HiRISE images ESP_038785_1390; 334.041^0 E, 40.881^0 S; res. 25 cm/pixel; PSP_007824_1420; 322.026^0 E, 37.895^0 S; res. 50cm/pixel; ESP_021734_1460; 353.240^0 E, 33.752^0 S; 25 cm/pixel; NASA/JPL/University of Arizona). **(d, also c, f)** Type 2(b) depressions: smaller scale than Type 2(a), rimmed and, often, clustered densely on the floor and walls of the latter ESP_021734_1460; 353.240^0 E, 33.752^0 S; 25 cm/pixel; NASA/JPL/University of Arizona). **(e, also b, d, f)** Type 2 lightly-toned and mantled-

terrain. Note the absence of cratering and the mutedness of the underlying topography (HiRISE image PSP_007824_1420; 322.026^0 E, 37.895^0 S; res. 50 cm/pixel; NASA/JPL/University of Arizona). **(f)** Type 2(a) depression incised by multiple Type 2(b) depressions, both of which overlie a Type 1 depression (as marked by the dark-toned and polygonised strip of terrain on the left-hand side of the image). Here the Type-2 mantle seemingly has contracted, possibly ablated, and revealed the underlying dark-toned Type-1 terrain that might not be visible otherwise (HiRISE image PSP_007033_1445; 321.183^0, E 35.000^0 S; 50 cm/pixel; NASA/JPL/University of Arizona). **(g-h)** Type 2(c) depressions: possible example of mantle degradation, with (g) showing less degradation than (h) (HiRISE images ESP_028552_1440; 339.485^0, E 35.640^0 S; 50cm/pixel; ESP_026851_1445; 333.395^0, E 35.002^0 S; 25 cm/pixel; NASA/JPL/University of Arizona). **(i)** Type 2(c) depressions on the ejecta of an impact crater (HiRISE image ESP_022315_1440; 330.846^0, E 35.843^0 S; 25 cm/pixel; NASA/JPL/University of Arizona).

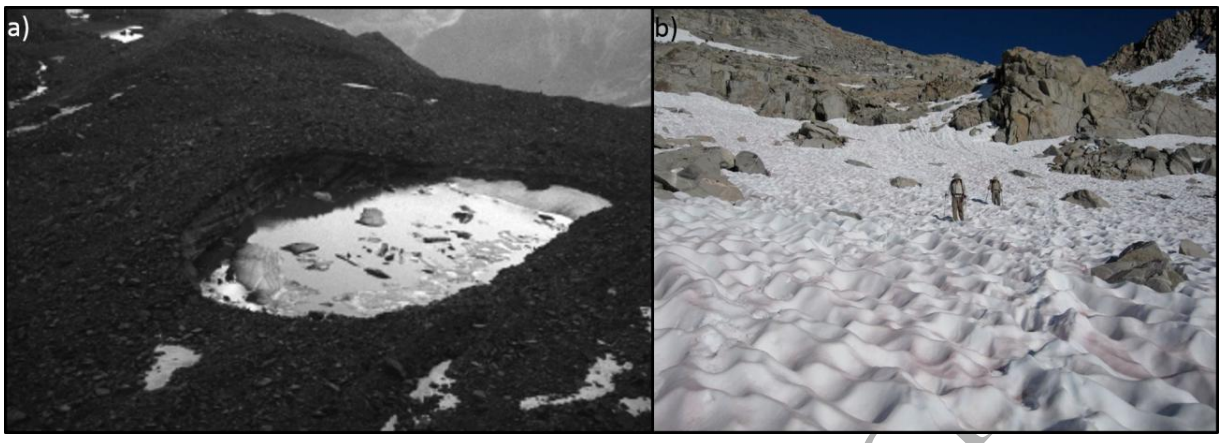

Fig. 5 Glacial (dead-ice) thermokarst-lake set in glacial debris/overburden (basin area = ~10,000m^2; the height of the ice-front to the left is >10m (Kääb and Haeberli, 2001; copyright by the Regents of the University of Colorado). Here, lake formation is triggered by thaw. We hypothesise that morphologically similar dead-ice features, i.e. thermokarst basins, could have formed in the AR by means of ice-sublimation. **(b)** Alpine suncups (Mather Pass, California). Image credit: http://www.ultralight backpacker.com/index.html.

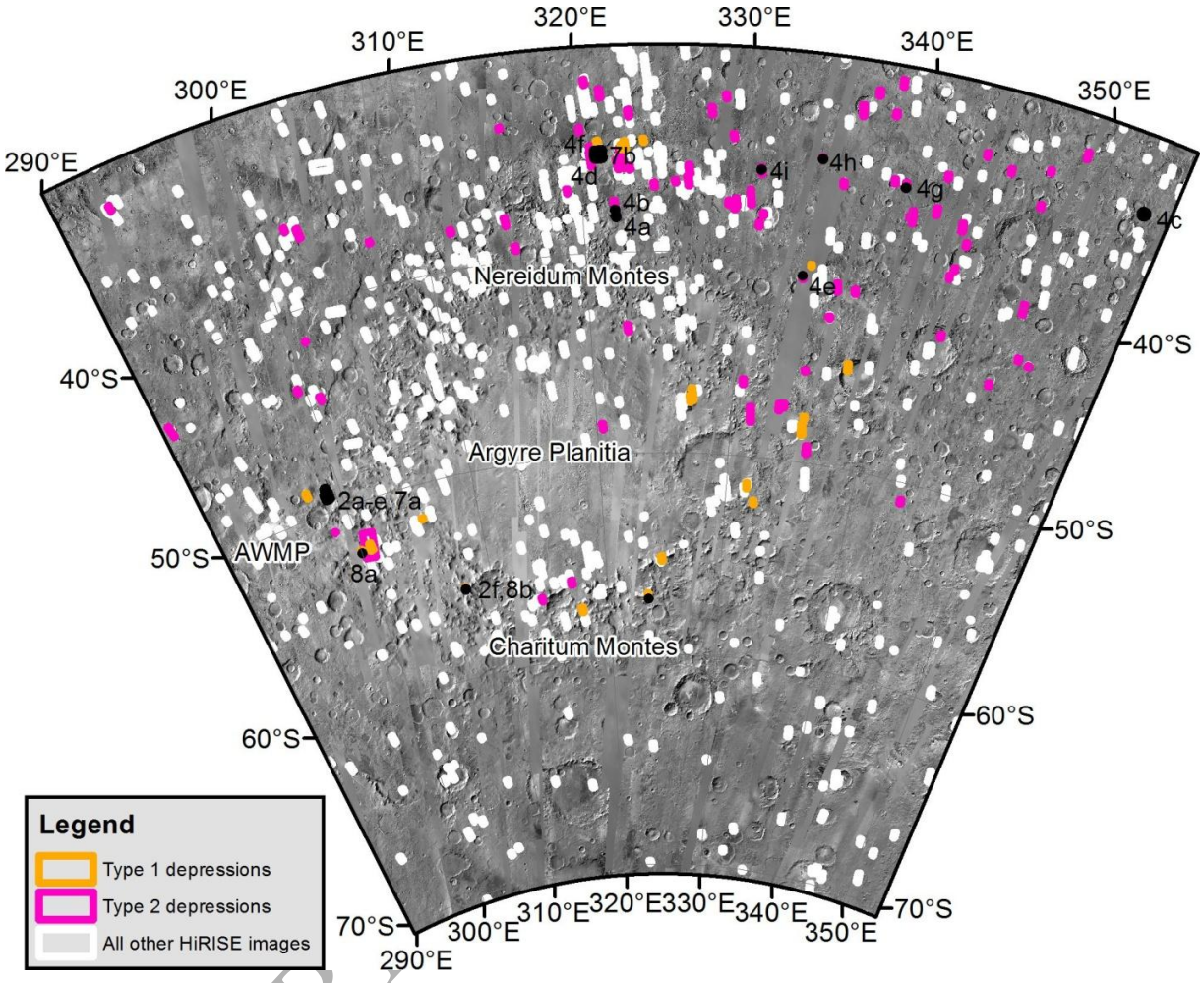

Fig. 6 Overview of the HiRISE images surveyed and the sites identified with Type-1 and Type-2 depressions. Background THEMIS-Day IR Global mosaic from ASU. The geographic locations of Figs. 2, 4, 7 and 8 and their sub-figures are shown and labelled in black.

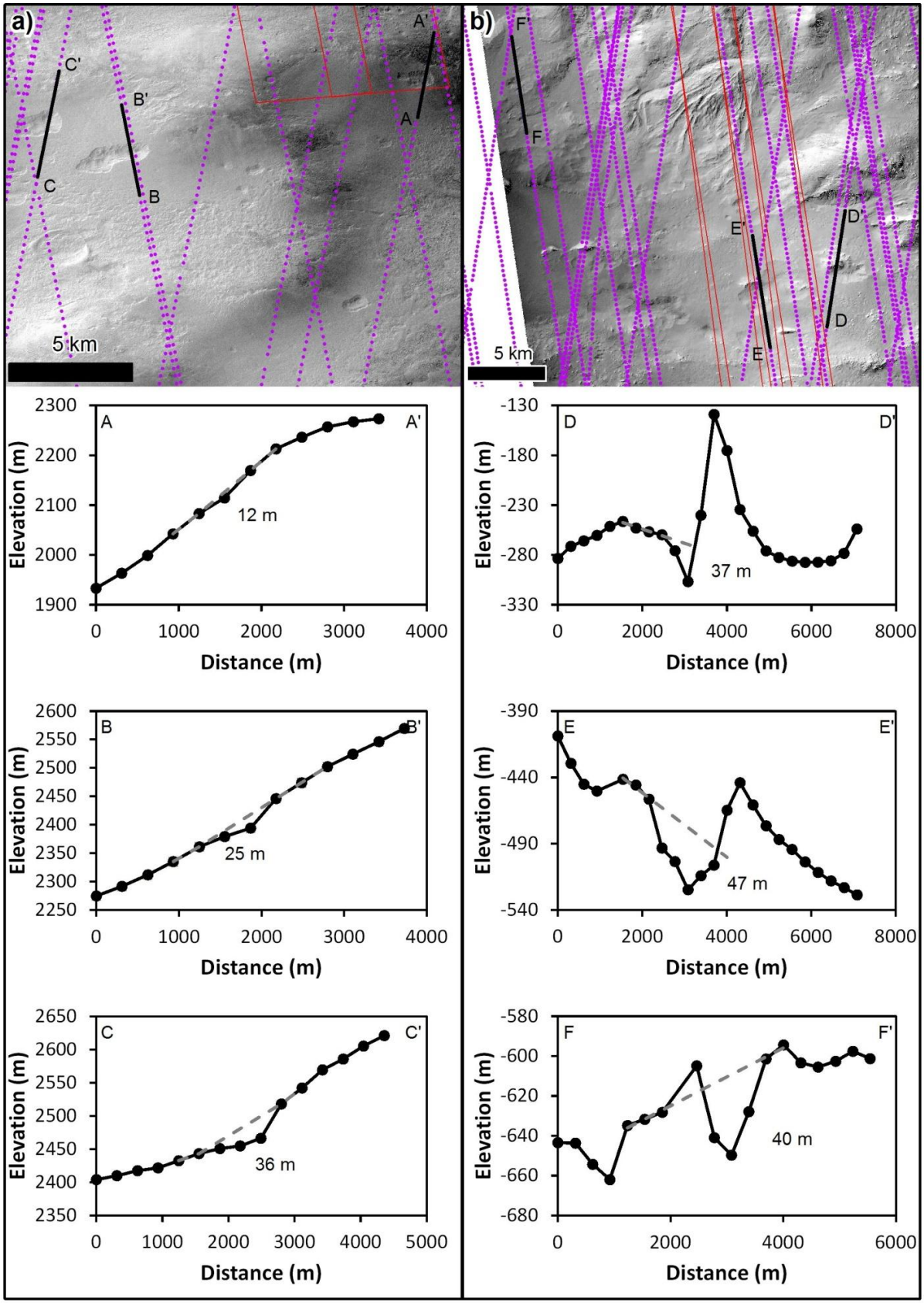
a)
A'
C'
B'
A
C
B
5 km
b)
F'
F
E'
D'
D
E
5 km
A
A'
12 m
Elevation (m)
Distance (m)
D
D'
37 m
Elevation (m)
Distance (m)
B
B'
25 m
Elevation (m)
Distance (m)
E
E'
47 m
Elevation (m)
Distance (m)
C
C'
36 m
Elevation (m)
Distance (m)
F
F'
40 m
Elevation (m)
Distance (m)

Fig. 7 Topographic profiles of Type-1 depressions with context images. On each topographic profile the black points are Mars Orbiter Laser Altimeter (MOLA) shots; the grey lines are linear interpolations across the depressions, using the three points adjacent to the depression boundary (excluding obvious non-mantled hills). Labels give the maximum distance between the interpolated line and the MOLA data. **(a)** CTX image B17_016132_1327_XN_47S061W with superposed MOLA shot points (in purple) obtained from the PDS; the outline of HiRISE image ESP_011319_1305 (in red) at site 6 and the locations of the topographic profiles shown below (in black). **(b)** CTX image P15_007033_1429_XN_37S038W with superposed MOLA shot points (in purple) obtained from the PDS; the outline of HiRISE images ESP_016197_1445 and PSP_007033_1445 (in red) at site 1; and, the locations of the topographic profiles shown below (in black).

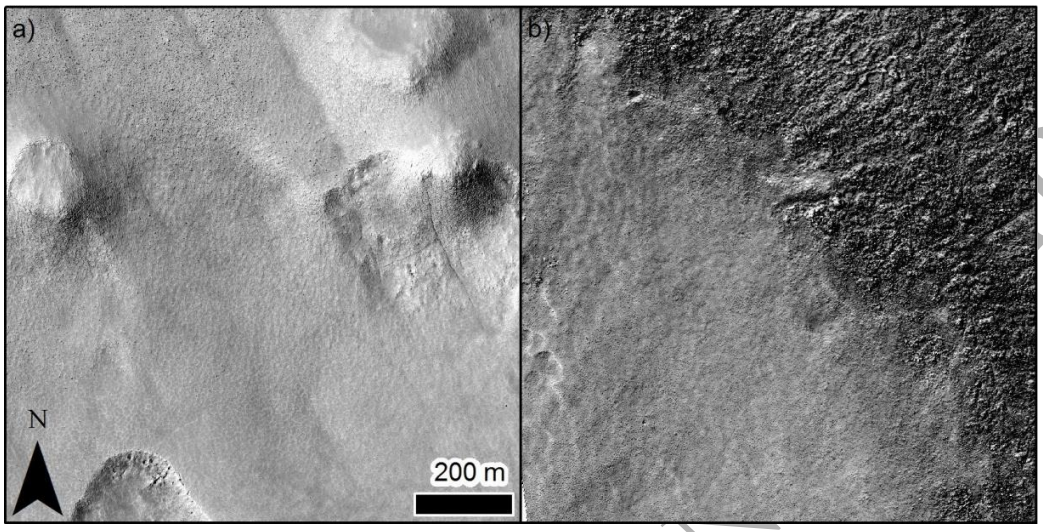

Fig. 8 (a) Mid-latitudinal valley floor covered by terrain that is smooth, i.e. mantled, albeit lineated; boulders are sparse (ESP_013890_1240; 307.523^{0}E, 55.615^{0}S; res. 50 cm/pixel; NASA/JPL/University of Arizona). **(b)** Mid-latitudinal mantled terrain in Charitum Montes; note the relatively steep and abrupt change of elevation where the putative mantle ends and the rocky terrain begins (ESP_032628_1275; 300.048^{0}E, 52.398^{0}S; res. 50 cm/pixel; NASA/JPL/University of Arizona).

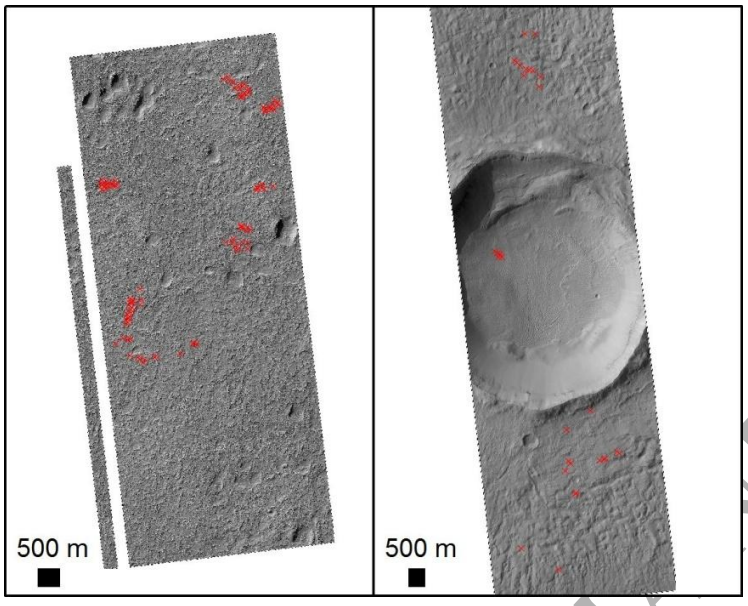

Fig. 9 HiRISE image ESP_026851_1445 (Table 2-location 22, solar incidence 76.7°), red crosses mark the locations where we made 100 random measurements of shadows cast by the walls of the Type-2c depressions. **(b)** HiRISE image ESP_028552_1440 (Table 2-location 27, solar incidence 66.892612°), red crosses mark the locations where 30 random measurements are made.

Table 1: Location and details of sites identified as having Type 1 depressions in this study.[a]

Image #	Location	Site	Image reference	cm/pixel	longitude	latitude	Gullies	Polygons	Unit(s)	Unit Name(s)
1	**1**		ESP_039392_1450	25	323.816	34.588	x	x	C1	Old crater materials
2	**2**		PSP_004976_1450	50	322.723	34.797	x	x	C1	Old crater materials
3	**3**	(a)	ESP_012874_1450	25	322.526	34.869	x	x	C1	Old crater materials

4		(b)	ESP_013019_1450	25	322.525	34.872	x	x	C1	Old crater materials
5	**4**	(a)	PSP_007033_1445	50	321.183	35.000		x	Nabr (and Nh2 in northernmost 10%, Cr in very SE)	Argyre basin and rim materials
6		(b)	ESP_016197_1445	50	321.184	35.004		x	Nabr (and Nh2 in northernmost 10%, Cr in very SE)	Argyre basin and rim materials
7	**5**		ESP_040974_1395	25	334.513	40.255	x	x	C1	Old crater materials
8	**6**		ESP_038521_1345	50	337.943	44.975		x	Cr and Cfs	Old crater materials and Smooth crater floor materials
9	**7**		PSP_006901_1325	50	327.104	47.078		x	NArb	Argye rim and basin materials
10	**8**		ESP_034829_1325	50	326.933	47.304	x	x	NArb	Argye rim and basin materials
11	**9**		ESP_034829_1325	50	326.933	47.304	x	x	NArb	Argye rim and basin materials
12	**10**		PSP_006993_1320	25	335.384	47.804	x	x	NAbr	Argyre basin and rim materials
13	**11**		PSP_002457_1310	25	335.305	48.208	x	x	NAbr	Argyre basin and rim materials
14	**12**		ESP_011911_1310	50	335.371	48.533	x	x	NAbr	Argyre basin and rim materials
15	**13**		PSP_001349_1310	50	335.336	48.578	x	x	NAbr	Argyre basin and rim materials
16	**14**		ESP_023925_1305	25	297.495	48.851		x	Nh1 and Hnb	Highlands member 1 and Highlands basins materials
17	**15**		ESP_011319_1305	50	298.954	49.001		x	Nh1	Highlands member 1
18	**16**		ESP_039049_1280	25	331.610	51.484	x	x	C2	Young crater materials
19	**17**		ESP_021960_1280	25	305.499	51.706		x	C1	Old crater materials
20	**18**		ESP_038640_1275	25	332.262	52.267	x	x	C2	Young crater materials
21	**19**	(a)	PSP_003711_1275	25	300.895	52.312		x	NAb1, NArb, NAr	Argyre basin member 1, Argye rim and basin materials, Argyre rim materials
22		(b)	PSP_005333_1275	25	300.902	52.324		x	NAb1, NArb, NAr	Argyre basin member 1, Argye rim and basin materials, Argyre rim materials
23	**20**	(a)	ESP_032628_1275	25	300.048	52.398		x	NAb1, NArb, NAr	Argyre basin member 1, Argye rim and basin materials, Argyre rim materials
24		(b)	ESP_032773_1275	25	300.049	52.399		x	NAb1, NArb, NAr	Argyre basin member 1, Argye rim and basin materials, Argyre rim materials
25	**21**		PSP_003922_1275	25	300.755	52.411	x	x	NAb1, NArb, NAr	Argyre basin member 1, Argye rim and basin materials, Argyre rim materials
26	**22**		PSP_005319_1245	25	324.839	55.273	x	x	NAr	Argyre rim materials
27	**23**		ESP_013890_1240	50	307.523	55.615		x	NAbr, NAr	Argyre basin and rim materials, Argyre rim materials
28	**24**		PSP_006176_1225	25	323.637	57.130		x	NArb	Argye rim and basin materials
29	**25**		PSP_002761_1220	25	317.578	57.610		x	NArb, NAb2, NAb3	Argye rim and basin materials, Argyre basin member 2, Argyre basin member 3

[a]"x" means the feature is present.

Table 2: Location and details of sites identified as having Type 2 depressions in this study.[a]

Image #	Location	Site	Image reference	cm/pixel	longitude	latitude	Gullies	Polygons
1	**1**	(a)	ESP_023396_1490	50	338.302	30.832	x	
2		(b)	ESP_024319_1490	50	338.300	30.834	x	
3	**2**	(a)	PSP_008153_1480	50	337.094	31.475	x	
4		(b)	PSP_009155_1480	50	337.095	31.475	x	
5		(c)	ESP_021695_1480	25	337.094	31.457	x	
6		(d)	ESP_022684_1480	50	337.096	31.485	x	
7	**3**		ESP_020232_1480	50	320.528	31.687	x	
8	**4**		ESP_017330_1475	50	349.176	31.991	x	
9	**5**		ESP_025758_1475	50	293.004	32.064		
10	**6**		ESP_027247_1470	50	321.371	32.249		
11	**7**	(a)	ESP_022895_1475	25	338.199	32.321	x	
12		(b)	ESP_022262_1475	25	338.199	32.322	x	
13	**8**	(a)	ESP_039286_1480	25	337.091	31.469	x	
14		(b)	ESP_027075_1475	25	338.194	32.348	x	
15		(c)	ESP_027774_1475	25	338.195	32.350	x	
16		(d)	ESP_038112_1475	25	338.196	32.350	x	
17		(e)	ESP_036345_1475	50	338.196	32.352	x	
18		(f)	ESP_031954_1475	25	338.204	32.354	x	
19		(g)	ESP_035501_1475	25	338.197	32.353	x	
20		(h)	ESP_037057_1475	50	338.198	32.356	x	
21		(i)	ESP_030820_1475	25	338.205	32.357	x	
22		(j)	ESP_032165_1475	25	338.205	32.358	x	
23		(k)	ESP_013836_1475	25	338.193	32.360	x	
24	**9**		PSP_008364_1475	50	336.325	32.433		
25	**10**		PSP_007916_1475	50	328.560	32.412		
26	**11**		ESP_034908_1465	50	327.791	33.121		
27	**12**	(a)	PSP_006756_1465	25	322.972	33.257		
28		(b)	ESP_023779_1465	25	322.977	33.263		
29	**13**		ESP_016262_1465	25	347.469	33.263	x	
31	**14**		ESP_028776_1465	25	343.720	33.324	x	
32	**15**		ESP_026733_1460	25	315.544	33.524		
33	**16**		ESP_021734_1460	25	353.240	33.752	x	
34	**17**		ESP_025466_1460	50	345.292	33.788		
35	**18**		ESP_034816_1460	50	320.094	33.966		
36	**19**	(a)	ESP_013098_1455	25	329.129	34.293	x	
37		(b)	PSP_004145_1455	25	329.123	34.305	x	
38	**20**		PSP_005806_1450	25	341.814	34.792		
39	**21**		ESP_028645_1450	50	320.647	34.882		
40	**22**		ESP_026851_1445	25	334.395	35.002		
41	**23**		ESP_017040_1445	50	347.511	35.017		
42	**24**		PSP_008114_1445	50	322.404	35.404	x	
43			ESP_017331_1440	50	322.647	35.730	x	

Image #	Location	Site	Image reference	cm/pixel	longitude	latitude	Gullies	Polygons
44	**25**		PSP_007679_1440	50	320.695	35.438		
45	**26**		PSP_007652_1440	25	338.813	35.540	x	
46	**27**		ESP_028552_1440	50	339.485	35.640	x	
48	**28**	(a)	ESP_022315_1440	25	330.846	35.843	x	
49		(b)	ESP_028038_1440	50	330.859	35.874	x	
50		(c)	ESP_036187_1440	50	330.858	35.875	x	
51		(d)	ESP_030517_1440	25	330.859	35.877	x	
52		(e)	ESP_028315_1440	25	330.860	35.879	x	
53	**29**	(a)	PSP_007468_1440	25	322.285	35.714	x	
54		(b)	PSP_006822_1440	25	322.285	35.720	x	
55	**30**		ESP_020166_1440	25	322.988	35.898		
56	**31**		PSP_008628_1435	50	326.543	35.986		
57	**32**		ESP_017436_1435	50	335.806	36.075		
58	**33**		ESP_030083_1435	50	301.948	36.084	x	
59	**34**		ESP_016501_1430	50	302.683	36.455	x	
60	**35**		ESP_025704_1430	50	326.490	36.555		
61	**36**		ESP_017594_1430	50	341.608	36.560	x	
62	**37**		PSP_010118_1430	50	325.712	36.581		
63	**38**		ESP_039115_1430	25	325.719	36.583		
64	**39**		ESP_040948_1430	25	324.416	36.738		
65	**40**		ESP_034104_1430	50	319.155	36.893		
66	**41**	(a)	ESP_015959_1425	25	340.227	37.010	x	
67		(b)	ESP_020706_1425	25	340.236	37.020	x	
68		(c)	PSP_007441_1425	50	340.232	37.098	x	
69	**42**		ESP_031176_1425	50	340.069	37.126	x	
70	**43**	(a)	PSP_006663_1425	25	343.355	37.034	x	
71		(b)	ESP_011436_1425	25	343.353	37.353	x	
72	**44**	(a)	ESP_039616_1420	25	329.319	37.535	x	?
73		(b)	ESP_039682_1420	25	329.316	37.524	x	?
74	**45**	(a)	ESP_025638_1425	50	330.327	37.195	x	
75		(b)	ESP_035264_1420	50	329.452	37.498	x	
76		(c)	ESP_026983_1420	50	329.451	37.516	x	
77		(d)	ESP_034341_1420	50	328.989	37.546	x	
78	**46**	(a)	ESP_016711_1420	50	329.360	37.610	x	
79		(b)	PSP_007771_1420	50	329.355	37.644	x	
80	**47**		ESP_013824_1420	25	306.731	37.801	x	
81	**48**		ESP_028420_1420	50	343.841	37.809		
82	**49**		PSP_007824_1420	50	322.026	37.895		
83	**50**		ESP_016078_1415	25	331.163	37.992	x	
84	**51**		ESP_026377_1415	50	315.180	38.081		
85	**52**		ESP_019995_1415	50	311.740	38.142		
86	**53**		ESP_038231_1410	50	330.955	38.513	x	

Image #	Location	Site	Image reference	cm/pixel	longitude	latitude	Gullies	Polygons
87	**54**		ESP_029765_1405	25	343.502	39.119		x
88	**55**		ESP_039721_1400	25	343.302	39.558	x	
89	**56**		PSP_008022_1405	50	315.598	39.425	x	
90	**57**		ESP_016829_1395	50	348.397	40.082		
91	**58**		ESP_040974_1395	25	334.513	40.255	x	x
92	**59**		ESP_038785_1390	25	334.041	40.881	x	?
93	**60**		ESP_029462_1385	50	336.370	41.136		
94	**61**	(a)	ESP_029963_1385	25	337.550	41.202	x	
95		(b)	ESP_030596_1385	25	337.554	41.212	x	
96	**62**		ESP_016211_1380	25	301.066	41.610	x	
97	**63**		ESP_016038_1370	25	343.722	42.478		
98	**64**		ESP_027167_1370	50	349.113	42.515		
99	**65**		ESP_041013_1370	25	349.907	42.657	x	
100	**66**	(a)	ESP_032086_1370	25	336.126	42.652	x	
101		(b)	ESP_032653_1370	25	336.155	42.658	x	
102	**67**		ESP_021855_1365	50	290.478	43.200		
103	**68**		ESP_037084_1360	50	322.576	43.780	x	
104	**69**		ESP_028514_1360	50	299.475	43.815		
105	**70**		PSP_004118_1355	25	347.701	44.138	x	
106	**71**		ESP_036887_1350	50	300.830	44.526		
107	**72**		ESP_032152_1340	25	335.015	45.473		
108	**73**		ESP_025071_1335	50	330.711	46.311		
109	**74**		ESP_034829_1325	50	326.933	47.304	x	
110	**75**	(a)	ESP_038917_1325	25	333.794	47.311	x	
111		(b)	ESP_029950_1325	25	333.483	47.399	x	
112	**76**		ESP_015933_1320	50	331.427	47.894		
113	**77**		ESP_032825_1310	25	320.439	48.617		
114	**78**	(a)	ESP_033299_1305	50	335.893	49.351		
115		(b)	ESP_024372_1305	50	335.910	49.345		
116	**79**		ESP_023475_1285	50	343.847	50.947		x
117	**80**		ESP_013587_1285	25	298.573	51.052		
118	**81**		AEB_000001_0150	25	300.769	52.203		
119	**82**	(a)	ESP_012848_1235	25	316.839	56.211		
120		(b)	ESP_012782_1235	25	316.838	56.218		
121	**83**		ESP_032377_1230	50	314.042	56.867		

[a]"x" means the feature is present and "?" means uncertain.